Preprints (www.preprints.org) | NOT PEER-REVIEWED | Posted: 24 March 2021 doi:10.20944/preprints202103.0589.v1

Article

Identification of LLDPE Constitutive Material Model for Energy Absorption in Impact Applications

Luděk Hynčík [1]*, Petra Kochová [2], Jan Špička [1], Tomasz Bońkowski [1], Robert Cimrman [1], Sandra Kaňáková [2], Radek Kottner [2] and Miloslav Pašek [3]

[1] New Technologies - Research Centre, University of West Bohemia, 301 00 Plzeň, Czech Republic; hyncik@ntc.zcu.cz (L.H.); spicka@ntc.zcu.cz (J. Š.); tomasz@ntc.zcu.cz (T. B.); cimrman3@ntc.zcu.cz (R. C.)
[2] Faculty of Applied Sciences, University of West Bohemia, 301 00 Plzeň, Czech Republic; kochovap@kme.zcu.cz (P.K.); kottner@kme.zcu.cz (R.K); kanaksan@kme.zcu.cz (S.K.)
[3] MECAS ESI s.r.o., Brojova 2113, 326 00 Plzeň, Czech Republic; Miloslav.Pasek@esi-group.com (M.P.)
* Correspondence: hyncik@ntc.zcu.cz

Abstract: Current industrial trends bring new challenges in energy absorbing systems. Polymer materials as the traditional packaging material seem to be promising due to their low weight, structure and production price. Based on the review, the linear low-density polyethylene material was identified as the most promising material for absorbing impact energy. The current paper addresses the identification of the material parameters and the development of a Constitutive material model to be used in future design by virtual prototyping. The paper deals with the experimental measurement of the stress-strain relations of the linear low-density polyethylene under static and dynamic loading. The quasi-static measurement is realized in two perpendicular principal directions and is supplemented by a test measurement in the 45 degrees direction, i.e. exactly between the principal directions. The quasi-static stress-strain curves are analyzed as an initial step for dynamic strain rate dependent material behavior. The dynamic response is tested in the drop tower using a spherical impactor hitting the flat material multi-layered specimen at two different energy levels. The strain rate dependent material model is identified by optimizing the static material response obtained in the dynamic experiments. The material model is validated by the virtual reconstruction of the experiments and by comparing the numerical results to the experimental ones.

Keywords: LLDPE; quasi-static and dynamic experimental tests, impact energy absorption; material parameter identification; constitutive material model; validation; simulation

1. Introduction

Thin-layered polymer materials are traditionally used for packaging goods to protect them during transportation. Therefore the major desired properties relate to thickness, density (which relates to weight), strengths, elongation, puncture resistance and stretching level, see Table 1. On the other hand, preliminary experimental tests show also a good performance of such materials in energy absorption.

Current trends in the automotive industry regarding future mobility bring new challenges for energy-absorbing safety systems. Non-traditional seating configurations in autonomous vehicles and complex crash scenarios including multi-directional loading are to be considered hand in hand with the advanced materials for energy absorption. Špička *et al.* (2019) used a numerical simulation approach in his study to assess the new safety system (see Figure 1) patented by Hanuliak (2018). The system is based on two layers of a multi-layered membrane injected from the roof between the windscreen and the frontal seats, catching the driver and the passenger during the accident, in a similar manner as airbag performs. The advantage of the approach over the airbag is a simple implementation for multi-directional impact loading and addressing the out-of-position seating issue.

As virtual prototyping plays an important role in the design of new products nowadays, the paper aims to identify the linear low-density polyethylene (LLDPE) material parameters for both static and dynamic loading, to implement them into a constitutive material model and to verify the material model by numerical simulations representing the experiments. As the static tests are represented by quasi-static loading conditions, the dynamic tests represent the scenario close to the one schematically described in Figure 1.

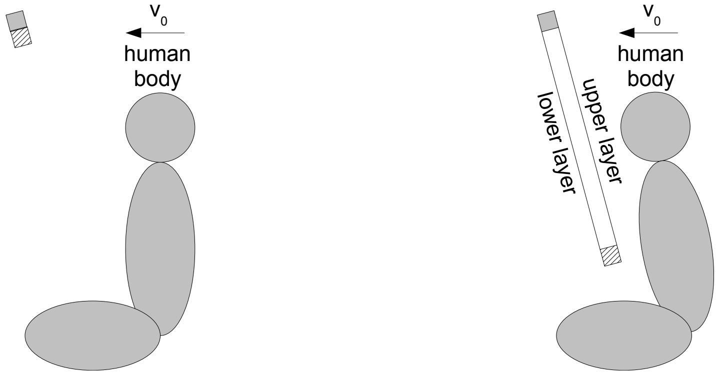

(**a**) Folded. (**b**) Unfolded.

Figure 1. Scheme of a new safety system for absorbing impact energy: **a**) Folded. **b**) Unfolded

LLDPE films have been identified as the most promising material in cases, where the impact loading is assumed, because of their higher average peak force and the energy to peak force when compared to LDPE [3]. LLDPE is a linear polyethylene with a significant number of short branches (see Figure 2) commonly made by copolymerization of ethylene and another longer olefin, which is incorporated to improve properties such as tensile strength or resistance to harsh environments. The structure of LLDPE leads to its heterogeneous non-linear behavior.

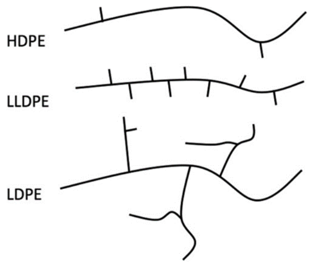

Figure 2. Chain structures of HDPE, LLDPE, and LDPE [4].

LLDPE is very flexible, elongates under stress, absorbs a high level of impact energy and thus is suitable to make thin and ultra-thin films [5–8]. The mechanical properties of polyethylene depend on its complex structure [9], which leads to a non-linear heterogeneous behavior during mechanical and numerical tests. This behavior was explained e.g. by Jordan *et al.* (2016), Ragaert *et al.* (2016) and Zhang *et al.* (2004), where the differences in the chain structures among the HDPE (high-density polyethylene), LLDPE, and LDPE (low-density polyethylene) are described. Ren *et al.* (2019) finds out that LLDPE film MD tear strength is dependent on the utilized comonomers (higher for hexene and octene-based resins whilst lower for butene-based resins). Dogru *et al.* (2018) and Dorigato *et al.* (2010) defines the Poisson ratio as $\nu = 0.44$ for LLDPE.

The main mechanical characteristics of polyethylene are the yield stress and the yield strain, corresponding to the point where the plastic non-recoverable deformation due to permanent changes in polymer chains starts. The yield stress and the yield strain of LLDPE depend on temperature and the strain rate [5,6,15]. The yield stress increases

Preprints (www.preprints.org) | NOT PEER-REVIEWED | Posted: 24 March 2021 doi:10.20944/preprints202103.0589.v1

while the yield strain decreases with the increasing strain rate [9]. The double yield point is also mentioned by Plaza *et al.* (1997). The relation between the yield stress, the temperature and the strain rate can be described by constitutive laws [5,6,9,17]. The temperature-dependent mechanical properties of thin-layered materials are also described by Luyt *et al.* (2021). By comparison among LDPE, LLDPE and HDPE, LLDPE showed greater rate sensitivity than the other two materials under both static and dynamic regions of a compression test [9].

The typical stress-strain relation as well as the strain-rate dependence are sketched in Figure 3. Whilst Du *et al.* (2018) states the tensile properties dependent on the strain rate, Omar (2013) shows, how the yield stress depends on the strain rate.

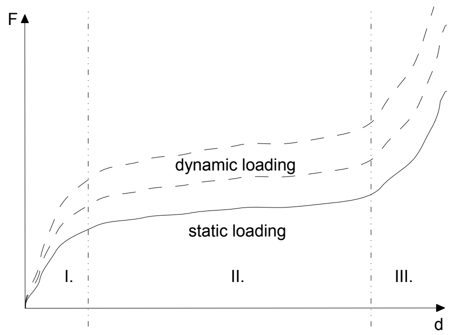

Figure 3. Typical stress-strain curve of LLDPE .

Durmus *et al.* (2008) shows the typical stress-strain curves of LLDPE as an initial elastic region I. followed by yielding that is accompanied by neck propagation in region II., see Figure 3. The third region III. is the stiffening leading to the material rupture.

LLDPE has anisotropic behavior due to its chain structure. The chain structure creates the anisotropy in 2 perpendicular directions, called the machine direction (MD) and the transversal direction (TD). The local preferential orientation of chains in LLDPE affects the tensile strength in MD and TD [11]. In the direction of the main chain orientation, mostly the MD, LLDPE are stiffer than in the perpendicular direction, mostly the TD [3,5,6,15]. The tensile stress-strain relations in MD and TD play an important role during the biaxial deformation of the impact test [3].

2. Materials and Methods

The material parameter identification is applied to the LLDPE thin foil produced by Tic (2020). Table 1 summarizes its parameters presented by the producer.

Table 1: LLDPE properties as produced by Tichelmann (2020).

Physical properties	Unit	Tolerance ±	Value	Testing method
Thickness	μm	2	12	Thickness gauge
Width	mm	5	500	Measuring tape
Length		-	5	High speed encoder
Density	g/cm^3	-	0.91 - 0.92	ASTM D-1505 [23]
Mechanical properties	Unit	Tolerance ±	Value	Testing method
Tensile strength MD	MPa	10	29.2	ASTM D-882 [23]
Tensile strength TD			14.1	
Break elongation MD	%		245	
Break elongation TD			540	
Dart drop	g		40	ASTM D-1709 [23]
Puncture	kg		1.7	High light tester
Stretching level	-	-	110	

 doi:10.20944/preprints202103.0589.v1

2.1. Quasi-static loading

The unilateral quasi-static loading test of the material sample was executed using the testing machine 574LE2 TestResources. From the material roll (see Figure 4) provided by the producer, the testing samples of length $l_0 = 5$ mm and width $w = 10$ mm were extracted, see Figure 5 (**a**), where the left and right yellow sides are fixed to the testing machine yaws. The thickness of the sample was $h = 12$ μm. The samples were fixed in the testing machine jaws (see Figure 5 (**b**)) and stretched in 2 major orthotropic directions (MD and TD). MD is in the direction, in which the material is winded up on the roll, whist TD is perpendicular to MD, see Figure 4.

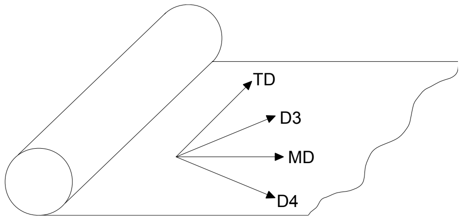

Figure 4. Sketch of the material roll.

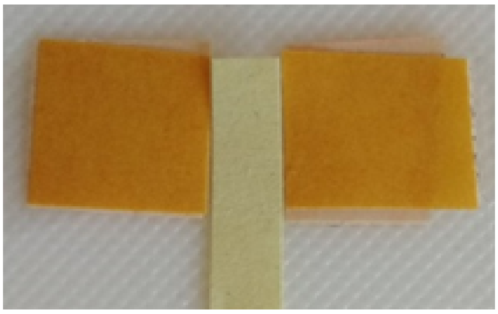

(**a**) Testing sample 5 mm × 10 mm.

(**b**) Testing jaws of 574LE2 TestResources.

Figure 5. Quasi-static test setup: (**a**) Testing sample. (**b**) Testing jaws.

Several samples were tested in each direction by three different stretching velocities v, namely 0.0002 m/s, 0.02 m/s and 0.2 m/s, half per each side of the jaws. Additional tests in the directions between MD and TD (labeled as D3 and D4, see Figure 4) were done to check the material behavior in the skewed (45 degrees) direction. Table 2 summarizes all the quasi-static tests. $N = 6$ samples were measured in each direction for each velocity except the $v = 0.2$ m/s, where D4 was already not necessary to be measured. The particular test finished when the sample ruptured.

Table 2: Quasi-static tests matrix.

Stretching velocity v [m/s]	Directions	Number of samples N
0.0002	MD	6
	TD	6
	D3	6
	D4	6
0.02	MD	6
	TD	6
	D3	6
	D4	6
0.2	MD	6
	TD	6
	D3	6

Preprints (www.preprints.org) | NOT PEER-REVIEWED | Posted: 24 March 2021 doi:10.20944/preprints202103.0589.v1

During the sample stretching, force F versus displacement d was recorded. Based on the sample size with the sample initial cross-sectional area $A_0 = hw$, the engineering stress σ versus engineering strain ϵ curves were calculated as

$$\sigma = \frac{F}{A_0}, \quad \epsilon = \frac{d}{l_0}. \tag{1}$$

The constant Young modulus E was also identified as the slope of the initial elastic region as

$$\sigma = \frac{F}{A_0} = E\frac{d}{l_0} \quad \Rightarrow \quad E = \frac{Fl_0}{dA_0}. \tag{2}$$

Fulfilling the aim of this study, the quasi-static tests were reproduced by numerical simulations. The simulation was realized in Virtual Performance Solution (VPS by ESI Group), version 2020. Following the structure of LLDPE in Figure 3 (2 mutually perpendicular sets of fibers), the material model 151 Fabric Membrane Element with Nonlinear Fibers [24] from the ESI constitutive material model database was proposed. According to the membrane theory, the stress resultant curves were calculated by multiplying the engineering stress by the membrane thickness as

$$\sigma_h = \sigma h \tag{3}$$

in both MD and TD. The resulting material curves taken as the average curves from the quasi-static test measurements in particular directions serve as the constitutive data to feed the material model 151. The model concerns 2 sets of fibers, whose stress versus strain relation is defined by engineering stress resultant versus engineering strain curve. The angle between the sets of fibers is 90 $^{\circ}$. The shear stress resultant necessary to complete the membrane material model was calculated using the measurement in direction D3 as shown in Figure 6.

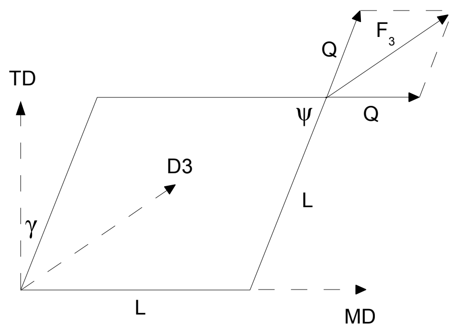

Figure 6. Evaluating the shear stress resultant.

Supposing a square sample, the shear force Q and shear angle γ are calculated through the following formulas.

$$Q = \frac{F_3}{2\cos\frac{\psi}{2}}, \tag{4}$$

where the shear angle

$$\gamma = \frac{\pi}{2} - \psi \tag{5}$$

is calculated based on the deformed sample angle ψ as

$$\cos\frac{\psi}{2} = \frac{\sqrt{2}L + d}{2L}, \tag{6}$$

Preprints (www.preprints.org) | NOT PEER-REVIEWED | Posted: 24 March 2021 doi:10.20944/preprints202103.0589.v1

where L is the side of the square sample, d is the displacement in direction D3 and F_3 is the force recorded in direction D3. Therefore the shear stress can be calculated as

$$\tau = \frac{Q}{Lh} \tag{7}$$

and the shear stress resultant is

$$\tau_h = \tau h = \frac{Q}{L}. \tag{8}$$

The thickness of the material is $h = 12\ \mu$m as defined by the producer [22]. The energy absorption was calculated from the dynamic experimental measurements and other numerical parameters feeding the material model were used as proposed by the VPS manual [24]. A single 4-nodal membrane element model was loaded by stretching both sides of the element by the 3 different loading velocities v, namely 0.0002 m/s, 0.02 m/s and 0.2 m/s, half per each side of the jaws, see Figure 7.

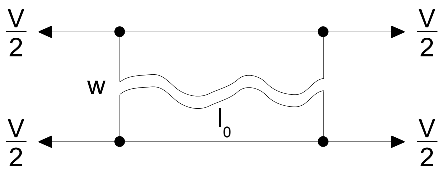

Figure 7. Single element quasi-static stretching simulation setup.

The element section force leading to the stress resultant was recorded during the simulation to be compared to the experimental data.

2.2. Dynamic loading

The dynamic tests, realized to reproduce the scenario from Figure 1, were in the form of drop tests of a spherical impactor falling with a given velocity on a multi-layered material sample. A special drop tower was designed for this purpose, see Figure 8.

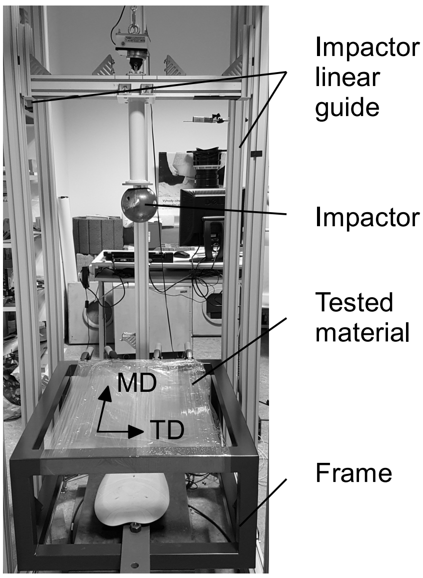

Figure 8. Drop tower.

According to Figure 1, the drop test was used to simulate the collision scenario similar to the impact of the human head into the safety layers during the frontal crash. Typical impacts for testing safety systems are designed for the velocities v_0 equal to 30 km/h and 50 km/h, corresponding to those used in sled tests. As the mass of the

Preprints (www.preprints.org) | NOT PEER-REVIEWED | Posted: 24 March 2021 doi:10.20944/preprints202103.0589.v1

human head is approximately $m = 4.5$ kg and the mass of the testing impactor is $M = 10.72$ kg, the drop test height H was calculated from the energy balance equation

$$\frac{1}{2}mv_0^2 = MgH \tag{9}$$

using the gravity acceleration $g = 9.81$ m/s^2. Equation (9) yields the drop heights equal to 1.49 m and 4.13 m for the velocities 30 km/h and 50 km/h, respectively. Due to the design limitations (limited maximum height of the drop tower), only the height $H = 1.5$ m corresponding to the velocity $v_0 = 30$ km/h was considered. To include different impact velocities for optimizing the constitutive material model, additional tests at the height $H = 1$ m corresponding to the velocity $v_0 = 25$ km/h were realized. Relating the energy balance with the head impactor mass $M = 10.72$ kg, the impact velocities corresponded to 4.43 m/s and 5.43 m/s for $H = 1$ m and 1.5 m, respectively.

As the dynamic impact loading was aggressive, the target material was wind up on the frame in several layers, see Figure 9. Preliminary experiments showed the sufficient number of layers n to be 8, 9 and 10, so the matrix of experiments contained 2 drop heights (10 dm and 15 dm) $\times$ 3 sets of layers (8, 9, and 10).

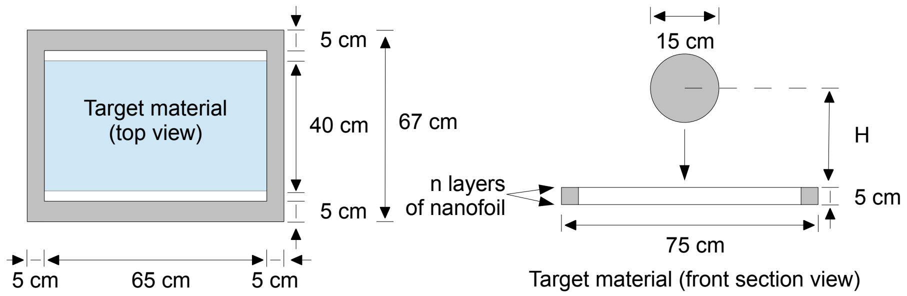

(**a**) Top over front view. (**b**) Side section.

Figure 9. Drop tower scheme: (**a**) Top over front view. (**b**) Side section.

Table 3 summarizing the drop tests shows that finally only 5 experimental drop tests were used for the optimization procedure, as the most aggressive one, meaning the fall from the highest height $H = 15$ dm to the lowest number of layers $n = 8$, ruptured the target material layers. The last column of Table 3 designates the identification of the particular drop tests in the following figures and analyses.

Table 3: Drop tests matrix.

Drop height H [dm]	Number of layers n	Optimization	Designation
10	8	✓	1008
	9	✓	1009
	10	✓	1010
15	8	× (material ruptured)	
	9	✓	1509
	10	✓	1510

The acceleration was measured using a uniaxial piezoelectric accelerometer Kistler 8742A5 fixed to the impactor, with the axis of the measurement parallel to the axis of the impactor. The impactor was held by an electromagnet and the free-fall motion was controlled by a linear guide, see Figure 9. Additionaly, the deflection of the impactor was measured with the laser measuring system Micro-Epsilon optoNCDT 2300-50 connected to the voltage input module NI 9215 in NI cDAQ-9178 Chassis. The final time-correlated signals were recorded by the NI Signal Express Software. The measured acceleration signal was filtered by the CFC 1000 filter [25]. From the physical principle, the piezoelec-

Preprints (www.preprints.org) | NOT PEER-REVIEWED | Posted: 24 March 2021 doi:10.20944/preprints202103.0589.v1

tric accelerometer cannot measure a free-fall gravity acceleration [26]. The experimental acceleration curve decreases to minus g just after releasing and reaches the equilibrium 0 g during the free fall, so the experimental acceleration curve needs to be adjusted to be comparable to the simulation results.

As the measured displacement was limited by the range of the laser measuring system, the double integration of the acceleration signal was used to extend the displacement in the whole time interval of the loading and unloading phases of the impact. Using the updated acceleration and displacement signals, the time-dependent total energy composed by the kinetic energy, the potential energy and the work done, respectively, were monitored as

$$E(t) = E_k + E_p + W = \frac{1}{2}Mv(t)^2 + Mgd(t) + \int_0^{d(t)} Ma(t)ds \tag{10}$$

to check the correctness of the calculations and to identify the energy absorption. Here $a(t)$ is the updated measured time-dependent impactor acceleration and the impactor velocity $v(t)$ and the impactor displacements $d(t)$ are calculated by the first and the second integration, respectively, of the acceleration signal $a(t)$. The gravity acceleration g is subtracted from the impactor acceleration to subtract the work done by the potential energy. Marking $E_{kp}(t) = E_k(t) + E_p(t)$ as the time-dependent sum of the kinetic and total energies, the energy absorption was calculated as the energy loss

$$D = 1 - \frac{\Delta E_u}{\Delta E_l}, \tag{11}$$

where $\Delta E_l = \max E_{kp}(t) - \min E_{kp}(t)|_{\text{loading}}$ is the energy difference during the loading phase and $\Delta E_u = \max E_{kp}(t) - \min E_{kp}(t)|_{\text{unloading}}$ is the energy difference during the unloading phase, where the resting energy is absorbed by the material work in order to have the constant total energy $E(t)$ from Equation (10).

2.3. Dynamic material parameters identification

As the material properties of LLDPE are strain-rate dependent [21], the constitutive material curves achieved by the quasi-static experimental measurements were used as the initial optimization step for dynamic material parameters optimization. The optimization was done using the numerical simulation reproducing the drop test experiment. The strain-rate dependent curves from the first optimization ($H = 10$ dm and $n = 8$ layers) were used as the initial curves for the other optimization runs to speed up the optimization process.

The standard MATLAB function *fminsearch* was adopted to optimize values for the stiffness and the yield stress in the two directions MD and TD towards the expected values. According to Figure 3, the stiffness of region I. and the yield stress were optimized. The MD and TD curves in region I. were updated as

$$\sigma_h^{\text{MD}} = k_y \sigma_h^{\text{MD}}\left(\frac{\epsilon_{\text{I.}}^{\text{MD}}}{k_1 k_e}\right), \quad k_1 = \begin{cases} \bar{k} & \forall \epsilon_{\text{I.}}^{\text{MD}} \in [0, \epsilon_{y1}^{\text{MD}}] \\ 1 & \forall \epsilon_{\text{I.}}^{\text{MD}} \in (\epsilon_{y1}^{\text{MD}}, \epsilon_{y2}^{\text{MD}}] \end{cases} \tag{12}$$

$$\sigma_h^{\text{TD}} = k_y \sigma_h^{\text{TD}}\left(\frac{\epsilon_{\text{I.}}^{\text{TD}}}{k_1 k_e}\right), \quad k_1 = \begin{cases} \bar{k} & \forall \epsilon_{\text{I.}}^{\text{TD}} \in [0, \epsilon_{y1}^{\text{TD}}] \\ 1 & \forall \epsilon_{\text{I.}}^{\text{TD}} \in (\epsilon_{y1}^{\text{TD}}, \epsilon_{y2}^{\text{TD}}] \end{cases} \tag{13}$$

by multiplying by dimensionless coefficients k_y, $\frac{1}{k_1}$ and $\frac{1}{k_e}$ during the optimization process. As the strain is divided by $k_1 k_e$, the coefficient $\frac{1}{k_1 k_e}$ is the stiffness multiplier in the region I. Dividing the region I. $[0, \epsilon_{y2}^{\text{MD,TD}}]$ by the first yield point $\epsilon_{y1}^{\text{MD,TD}}$, k_1 stiffens only the first part of the region I. by a constant $\bar{k}$ till the first yield point is reached. Coefficient k_y is the yield stress multiplier.

The optimization process was run in a loop controlled by a MATLAB script updating the constitutive material curves in MD and TD according to Equations (12) and (13). The cost function in the optimization measured the relative acceleration error E_a defined as

$$E_a = \frac{\|a_s(t) - a_e(t)\|}{\|a_e(t)\|}\Big|_{t\in[t_1,t_2]}, \tag{14}$$

noindent where $a_e(t)$ is the time-dependent acceleration signal measured from the experiment, $a_s(t)$ is the time-dependent acceleration response calculated by the numerical simulation and t is the time in the error calculation interval $[t_1, t_2]$. As well as the experimental acceleration signal, the calculated acceleration signal was also filtered by the CFC 1000 filter [25]. Figure 10 shows the simulation setup for optimization runs. The initial prestrain of the material wound on the frame was estimated based on preliminary numerical simulations to be 10 %, i.e. ϵ_0 =0.1 in MD. The displacement error E_d was calculated similarly to the acceleration error as

$$E_d = \frac{\|d_s(t) - d_e(t)\|}{\|d_e(t)\|}\Big|_{t\in[t_1,t_2]}, \tag{15}$$

where $d_e(t)$ is the time-dependent displacement signal obtained by the double integration of the acceleration signal and $d_s(y)$ is the time-dependent displacement response calculated by the numerical simulation.

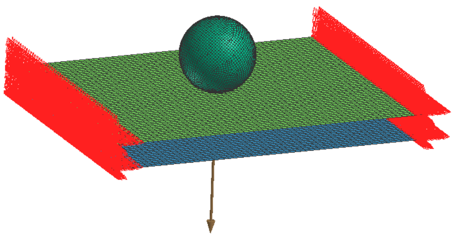

Figure 10. Drop test simulation setup.

For each testing scenario with n layers, the material is modeled by a single-layered membrane elements, where the number of upper and lower layers of the model is specified using the membrane material thickness defined by multiplying the single-layer thickness h by the number of layers n meaning also, that the stress resultant curves in Equations (3) and (8) are also multiplied by n for the particular model. Both sides of the layers are fixed by boundary conditions representing the attachment to the frame. The spherical impactor is modeled as a rigid body situated just above the upper layer and loaded by the initial velocity v corresponding to the particular height. The vertical acceleration and the vertical displacement are stored and compared to the experimental data.

3. Results

The following figures and tables summarize the results from the quasi-static tests as well as the identification of LLDPE parameters under dynamic loading.

3.1. Quasi-static loading

The quasi-static experiments prove that the typical stress versus strain curve for LLDPE is composed of three regions [21], see Figure 3. The summary of all results obtained by static experimental measurements under different quasi-static loading velocities using a single material layer is displayed in Figure 11. The curves are cut at positions of sample ruptures.

Preprints (www.preprints.org) | NOT PEER-REVIEWED | Posted: 24 March 2021 doi:10.20944/preprints202103.0589.v1

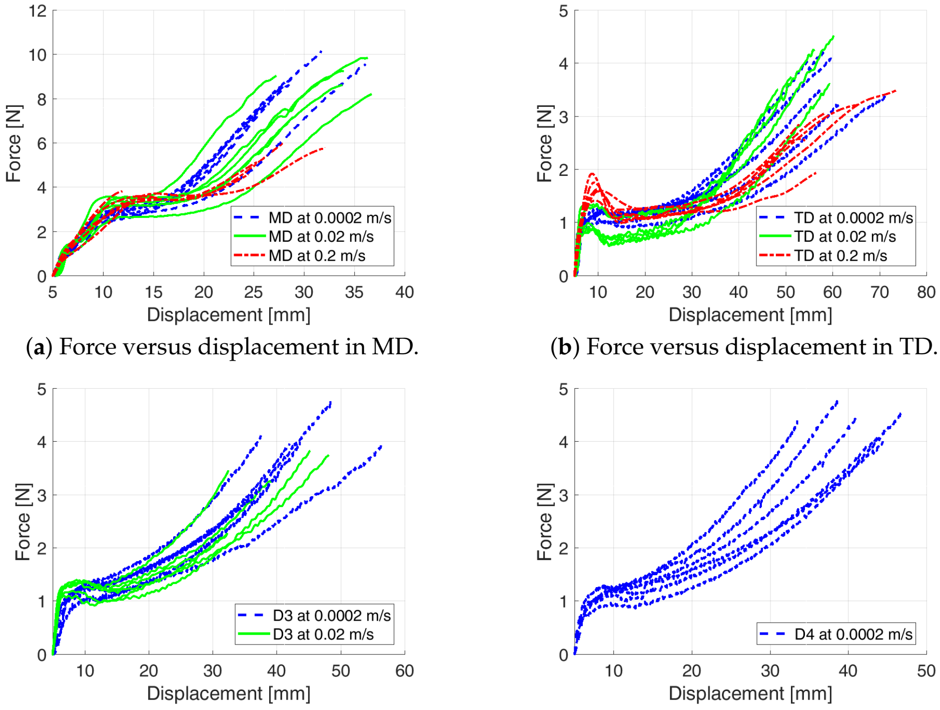

(**a**) Force versus displacement in MD. (**b**) Force versus displacement in TD.

(**c**) Force versus displacement in D3. (**d**) Force versus displacement in D4.

Figure 11. Material response in all directions: (**a**) MD. (**b**) TD. (**c**) D3. (**d**) D4.

Table 4 compares the measured experimental properties to those defined by Tic (2020).

Table 4: Material properties.

Direction	MD		TD	
Variable	Tensile stress [MPa]	Break elongation [%]	Tensile stress [MPa]	Break elongation [%]
Data sheet [22]	29.2	245	14.1	540
Experiment	29.3	139	16.2	701
Error [%]	0.5	-43	15	30

As the quasi-static tests in all three stretching velocities show similar performance, the curves for each direction were averaged as shown in Figure 12. It can be seen that the stretching responses in the skewed directions D3 and D4 fit between the MD and TD curves, so no unpredictable behaviour during the multi-directional loading should be expected. Therefore the skewed direction D3 was also used to identify the shear behavior according to Equations (4) – (8).

Whilst Figure 12 (**a**) shows the force dependent on the displacement averaged per the direction and per the stretching velocity, Figure 12 (**b**) shows the total average of the calculated stress versus strain curves in MD and TD calculated using Equation (1) for each quasi/static test measurement.

Preprints (www.preprints.org) | NOT PEER-REVIEWED | Posted: 24 March 2021 doi:10.20944/preprints202103.0589.v1

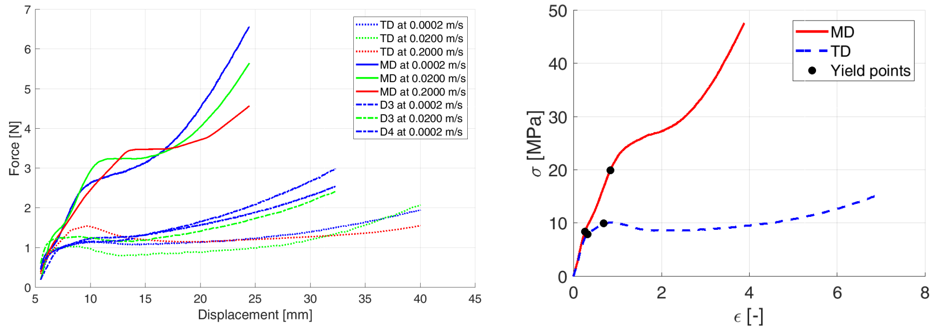

(**a**) Force versus displacement. (**b**) Stress versus strain.

Figure 12. Averaged constitutive material model curves: (**a**) Force versus displacement averaged per direction in all stretching velocities. (**b**) Stress versus strain averaged per direction.

By detailed analysis of the measured data in Figure 12 (**b**), the double yield point [16] is observed in both directions. In MD, the first point appears at the stress $\sigma_{y1}^{MD} = 8.4$ MPa, which corresponds to the strain $\epsilon_{y1}^{MD} = 0.26$. The second yield point appears by reaching the stress $\sigma_{y2}^{MD} = 20$ MPa, which corresponds to the strain $\epsilon_{y2}^{MD} = 0.84$. In TD, the first yield point appears at the stress $\sigma_{y1}^{TD} = 8$ MPa, which corresponds to the strain $\epsilon_{y1}^{TD} = 0.33$. The second yield point appears before reaching the maximum stress in region I. at the stress $\sigma_{y2}^{TD} = 10$ MPa corresponding to the strain $\epsilon_{y2}^{TD} = 0.69$. Table 5 summarizes the yield points.

Table 5: Yield points (σ_{hy} means the yield stress resultant).

Yield point	MD			TD		
	ϵ_y [-]	σ_y [MPa]	σ_{hy} [N/mm]	ϵ_y [-]	σ_y [MPa]	σ_{hy} [N/mm]
1	0.26	8.4	0.1	0.33	8	0.1
2	0.84	20	0.24	0.69	10	0.12

Taking into account the elastic region, the Young modulus $E = 50$ MPa is identified using Equation (2) by averaging the slopes of the elastic regions of all curves, see Table 6. The average was calculated for the particular directions and stretching velocities firstly leading to the global average. Both directions MD and TD are averaged as they exhibit similar stiffness in the first region.

Table 6: Young modulus.

Direction	MD						TD					
Stretching velocity v [m/s]	0.0002		0.02		0.2		0.0002		0.02		0.2	
Young modulus E [Mpa]	44	63	63	67	36	42	54	76	55	41	35	26
	57	76	63	47	37	50	39	53	64	47	31	30
	63	41	81	70	31	30	55	44	49	58	27	38
Young modulus	57		65		38		53		52		31	
			53						46			
E [Mpa]	50											

Finally, the constitutive material stress resultant curves developed using Equations (3) and (8) for a single layer of LLDPE were calculated for the quasi-static loading to feed

Preprints (www.preprints.org) | NOT PEER-REVIEWED | Posted: 24 March 2021 doi:10.20944/preprints202103.0589.v1

the constitutive material model, see Figure 21. A single-element numerical simulation to reproduce the stretching was run. Figure 13 shows perfect fit to the experimental curves.

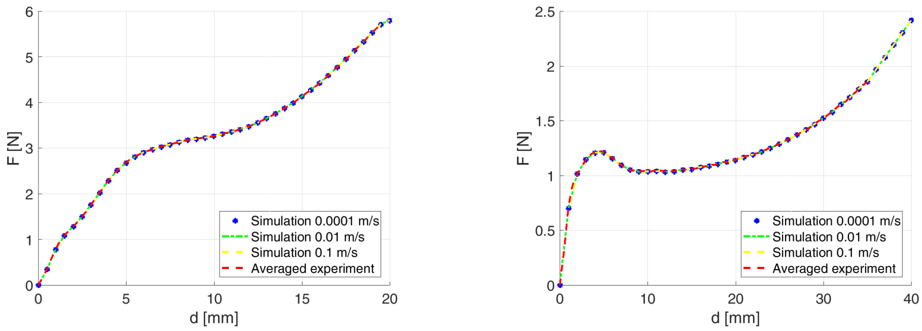

(**a**) Force versus displacement of a single element in MD.

(**b**) Force versus displacement of a single element in TD.

Figure 13. Performance of a single element model: (**a**) MD. (**b**) TD.

3.2. Dynamic loading

The acceleration decrease interval from 0 g to minus g approximately within the first 32 ms was used as the approximated parabolic acceleration ramp (see Figure 14) after the first contact of the impactor, where the mirrored signal from minus g to 0 g was added to the measured acceleration at the first 50 ms after the first contact between the impactor and the material, see Figures 15 – 19. By this the inability of the acceleration sensor to measure the free fall acceleration was mitigated.

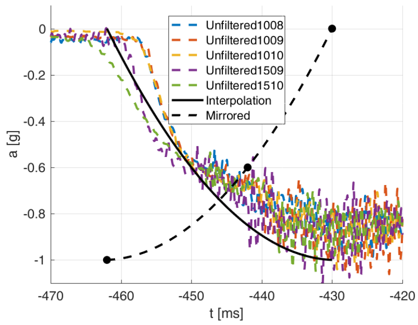

Figure 14. Gravity acceleration ramp.

The time of the first contact of the impactor to the material as well as the impact velocity were estimated from the ideal free fall from the height H after releasing the electromagnet. Due to uncertainty in the frame versus impactor linear guide friction, the related actual impact velocity and time of contact, an iterative process starting from the free fall assumptions was used to determine the actual moment of impact and the impact velocity, based on comparing the doubly integrated accelerations to the displacements obtained by the laser measuring system.

Such process led to a perfect fit in both measured and calculated displacements (both shown in Figures 15 – 19) identifying also the real impact velocity (see Table 7). The only exception was scenario 1509, where the displacement measurement failed. So the impact velocity was estimated to fit the remaining part of the displacement curve.

The dynamic loading proved the strain-rate dependency of LLDPE. LLDPE also exhibits strong energy absorption. The energy absorption was calculated by Equation (11) and was identified as being similar for all five drop test scenarios and averaged per drop height to obtain the final average $D = 88.96$ % (see Table 7) used for the constitutive material model.

Preprints (www.preprints.org) | NOT PEER-REVIEWED | Posted: 24 March 2021 doi:10.20944/preprints202103.0589.v1

Table 7: Energy absorption.

Drop height H [dm]	10			15	
Number of layers n	8	9	10	9	10
Impact velocity v [m/s]	4.16	4.14	4.18	4.94	5.01
Energy absorption D [%]	90.03	88.26	87.61	89.13	89.43
Energy absorption $\overline{D}$ [%]	88.63			89.28	
			88.96		

3.3. *Dynamic material parameters identification*

Several approaches to optimize the strain-rate dependent constitutive material curves were used and finally, the same stiffening ratio in MD and TD was proposed. The optimization process controlled by a MATLAB script involved running a series of simulations for updating the constitutive material model curves. The quasi-static response was taken as the initial guess for the optimization.

Table 8 shows the coefficients coming from the optimization process. Table 8 also shows the number of iterations leading to the optimized constitutive material curves as well as the errors from the cost function calculated by Equation (14) and the error in the displacement calculated by Equation (15).

Table 8: Optimised coefficients.

Drop height H [dm]	10			15	
Number of layers n	8	9	10	9	10
Number of iterations	278	152	205	234	221
First part stiffness multiplier k_1 [-]	2.75	2.89	2.99	3.14	3.07
Stiffness multiplier k_e [-]	3.41	3.47	3.55	1.69	2.29
Yield stress multiplier k_y [-]	1.00	0.91	0.88	1.16	1.04
Acceleration error E_s [%]	3	3	2	2	3
Displacement error E_d [%]	1	1	1	0	1

The intervals for calculating acceleration error are limited in Figures 15 – 19 by red dotted vertical lines to consider only the loading, where the iterative processes for the particular drop heights and the particular number of layers are shown.

The original experimental curves are in red dashed lines, the updated target curves (displacement obtained by integration and acceleration updated by the gravity) are shown in black dashed color, the initial curves (using the static constitutive material model) for optimization iterations are shown in blue dashed lines, the optimized curves are shown in blue solid lines and the iterative process is shown by solid grey curves.

Preprints (www.preprints.org) | NOT PEER-REVIEWED | Posted: 24 March 2021 doi:10.20944/preprints202103.0589.v1

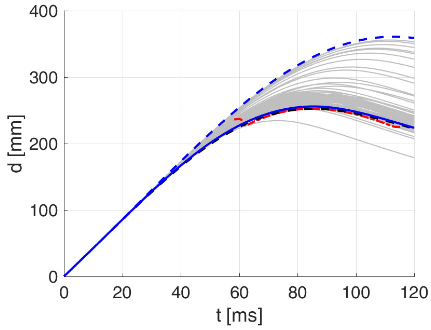

(**a**) Impactor displacement.

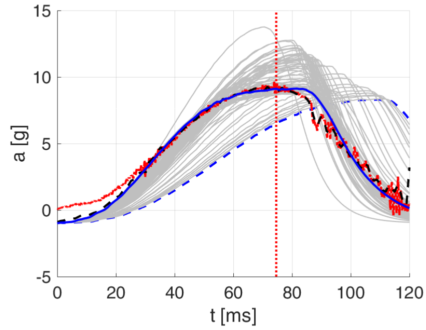

(**b**) Impactor acceleration.

Figure 15. Optimisation iterations for the drop height $H = 10$ dm and $n = 8$ layers: (**a**) Displacement. (**b**) Acceleration.

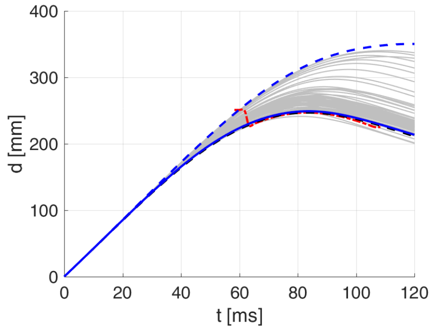

(**a**) Impactor displacement.

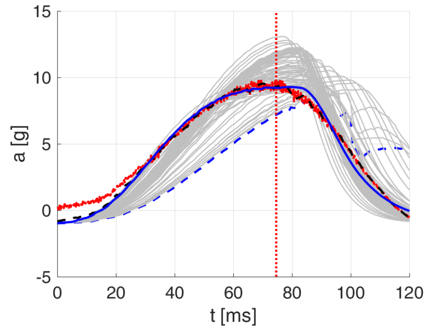

(**b**) Impactor acceleration.

Figure 16. Optimisation iterations for the drop height $H = 10$ dm and $n = 9$ layers: (**a**) Displacement. (**b**) Acceleration.

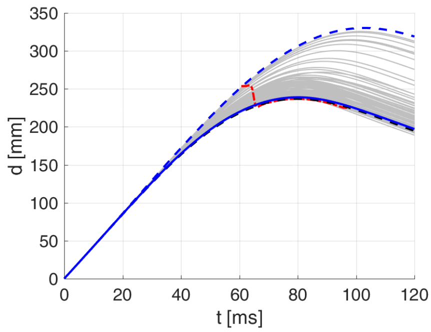

(**a**) Impactor displacement.

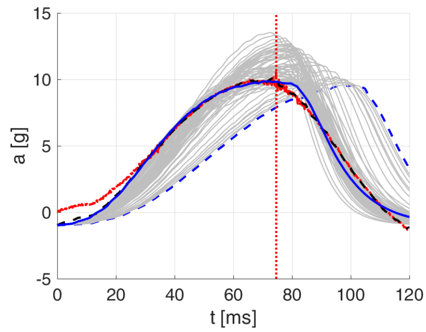

(**b**) Impactor acceleration.

Figure 17. Optimisation iterations for the drop height $H = 10$ dm and $n = 10$ layers: (**a**) Displacement. (**b**) Acceleration.

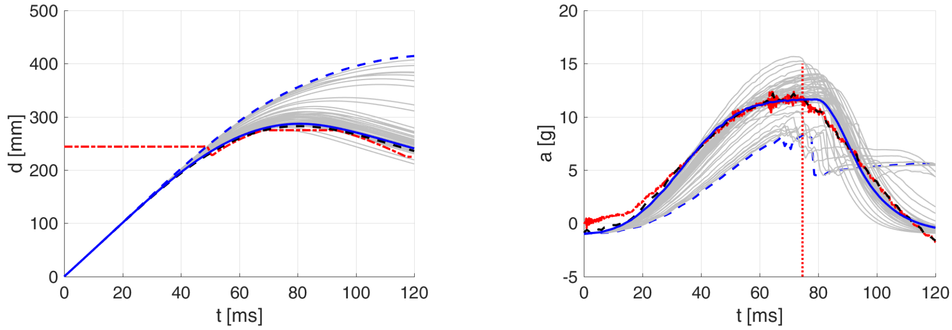

(**a**) Impactor displacement. (**b**) Impactor acceleration.

Figure 18. Optimisation iterations for the drop height $H = 15$ dm and $n = 9$ layers: (**a**) Displacement. (**b**) Acceleration.

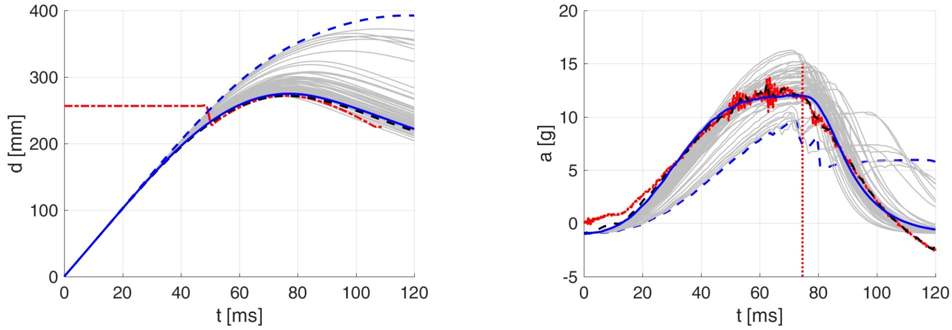

(**a**) Impactor displacement. (**b**) Impactor acceleration.

Figure 19. Optimisation iterations for the drop height $H = 15$ dm and $n = 10$ layers: (**a**) Displacement. (**b**) Acceleration.

All the identified strain-rate dependent engineering stress resultant versus engineering strain constitutive material curves in both MD and TD are show in Figure 20 (**a**). Due to the two different drop heights and three different sets of multi-layers, each drop scenario provides a different strain-rate dependent response, so all tests were normalized by the number of layers, which leads to similar strain-rate constitutive material curves for a single layer is both MD and TD, see Figure 20 (**b**).

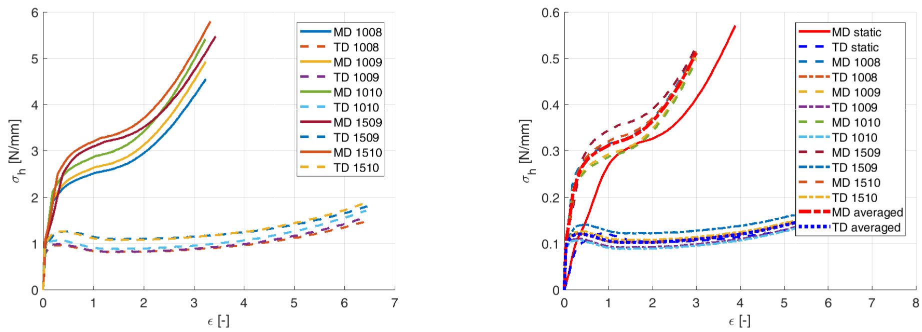

(**a**)Particular drop test particular drop tests. (**b**) Particular drop test reponse per layer.

Figure 20. Strain-rate dependent constitutive material model curves: (**a**) For particular tests. (**b**) Per layer.

As the difference between the curves corresponds to the difference during the experimental measurement, the constitutive material curves in MD and TD are identified by averaging the drop tests, see Figure 21 (**a**). Figure 21 (**b**) shows the shear stress versus shear strain as calculated by Equations (3) – (8) for a single layer.

 doi:10.20944/preprints202103.0589.v1

Using the identified averaged constitutive material curves in both MD and TD and the average energy absorption, all drop tests were reconstructed by numerical simulations. The results are shown in Figures 22 – 26.

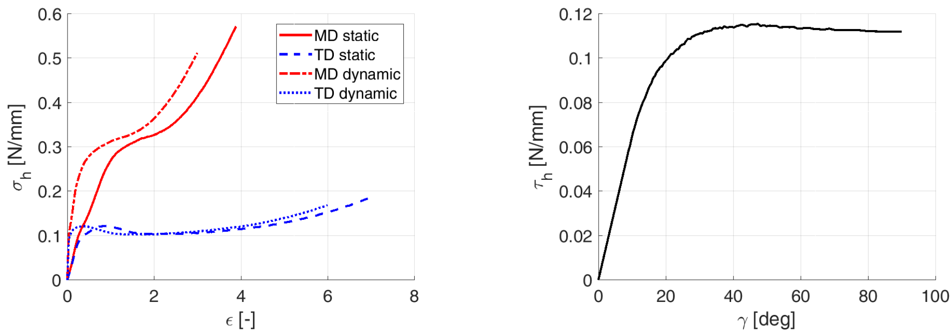

(**a**) Stress resultant versus strain in MD/TD. (**b**) Shear stress resultant versus shear strain.

Figure 21. Averaged strain-rate dependent constitutive material model curves: (**a**) Major directions. (**b**) Shear.

Table 9 shows the agreement in acceleration and displacement for all the drop tests using the averaged constitutive material curves.

Table 9: Final results.

Drop height H [dm]	10			15	
Number of layers n	8	9	10	9	10
Acceleration error E_s [%]	6	8	10	6	3
Displacement error E_d [%]	5	2	2	3	2

Figure 22 compares the simulation to the experimental drop test for the drop height $H = 10$ dm and the number of layers $n = 8$. Figure 23 compares the simulation to the experimental drop test for the drop height $H = 10$ dm and the number of layers $n = 9$. Figure 24 compares the simulation to the experimental drop test for the drop height $H = 10$ dm and the number of layers $n = 10$. Figure 25 compares the simulation to the experimental drop test for the drop height $H = 15$ dm and the number of layers $n = 9$. Figure 26 compares the simulation to the experimental drop test for the drop height $H = 15$ dm and the number of layers $n = 10$.

Preprints (www.preprints.org) | NOT PEER-REVIEWED | Posted: 24 March 2021 doi:10.20944/preprints202103.0589.v1

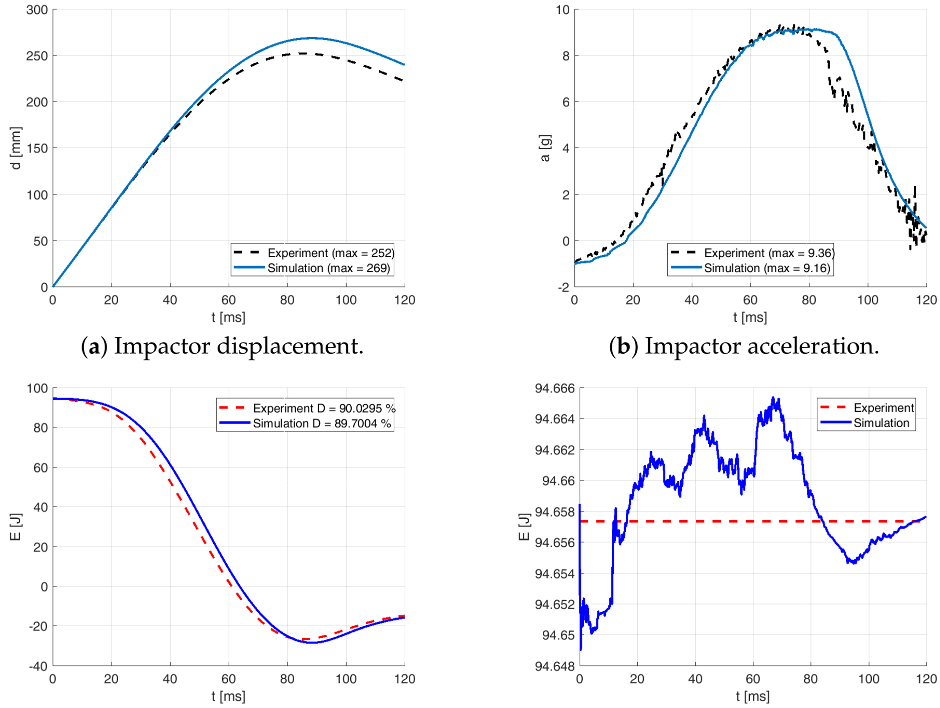

(**a**) Impactor displacement. (**b**) Impactor acceleration.

(**c**) Impactor energy loss. (**c**) Impactor total energy.

Figure 22. Comparison of drop test simulation to experiment for the drop height $H = 10$ dm and $n = 8$ layers: (**a**) Displacement (**b**) Acceleration. (**c**) Energy loss. (**d**) Total energy.

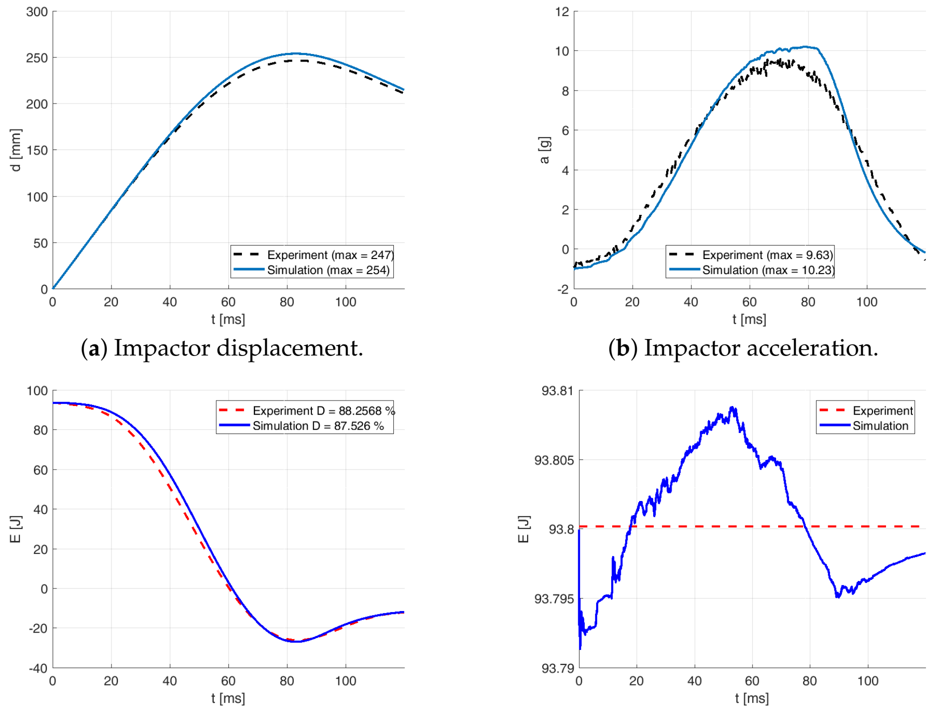

(**a**) Impactor displacement. (**b**) Impactor acceleration.

(**c**) Impactor energy loss. (**c**) Impactor total energy.

Figure 23. Comparison of drop test simulation to experiment for the drop height $H = 10$ dm and $n = 9$ layers: (**a**) Displacement (**b**) Acceleration. (**c**) Energy loss. (**d**) Total energy.

Preprints (www.preprints.org) | NOT PEER-REVIEWED | Posted: 24 March 2021 doi:10.20944/preprints202103.0589.v1

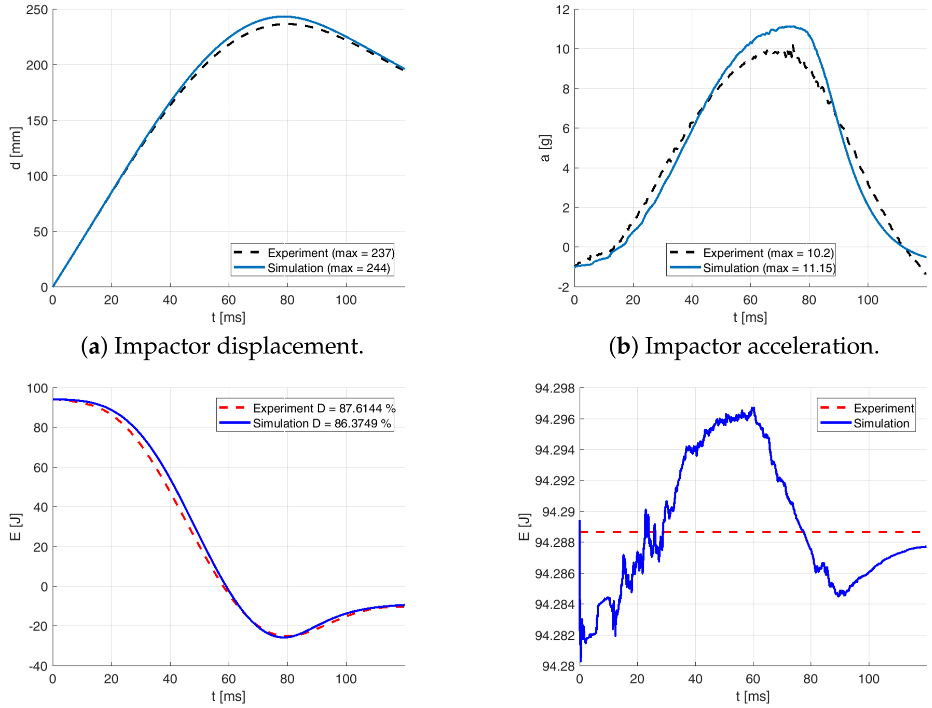

(**a**) Impactor displacement. (**b**) Impactor acceleration.

(**c**) Impactor energy loss. (**c**) Impactor total energy.

Figure 24. Comparison of drop test simulation to experiment for the drop height $H = 10$ dm and $n = 10$ layers: (**a**) Displacement (**b**) Acceleration. (**c**) Energy loss. (**d**) Total energy.

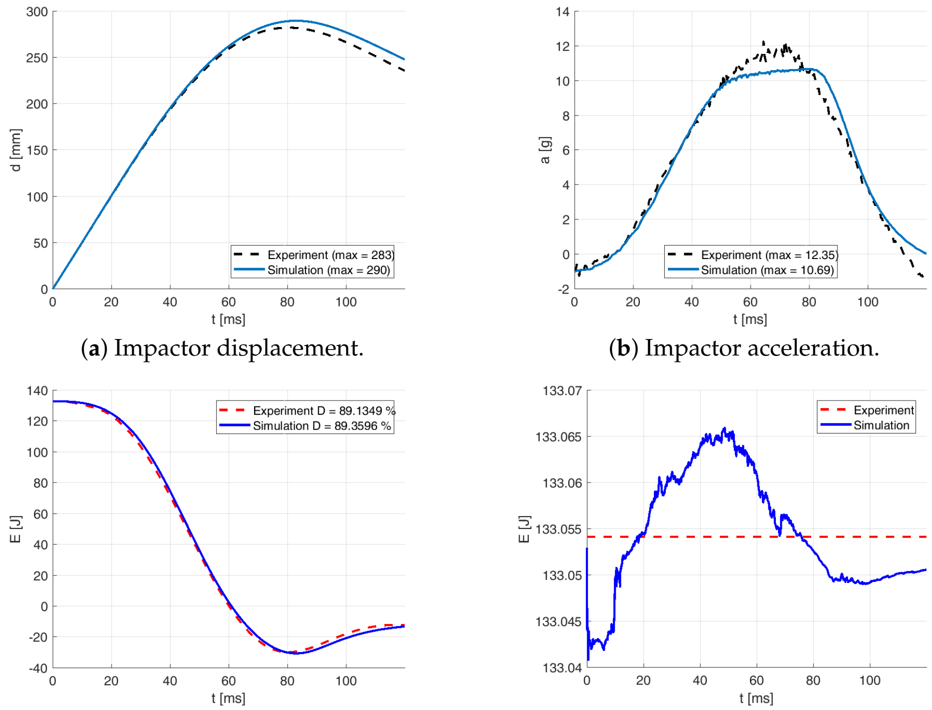

(**a**) Impactor displacement. (**b**) Impactor acceleration.

(**c**) Impactor energy loss. (**c**) Impactor total energy.

Figure 25. Comparison of drop test simulation to experiment for the drop height $H = 15$ dm and $n = 9$ layers: (**a**) Displacement (**b**) Acceleration. (**c**) Energy loss. (**d**) Total energy.

Preprints (www.preprints.org) | NOT PEER-REVIEWED | Posted: 24 March 2021 doi:10.20944/preprints202103.0589.v1

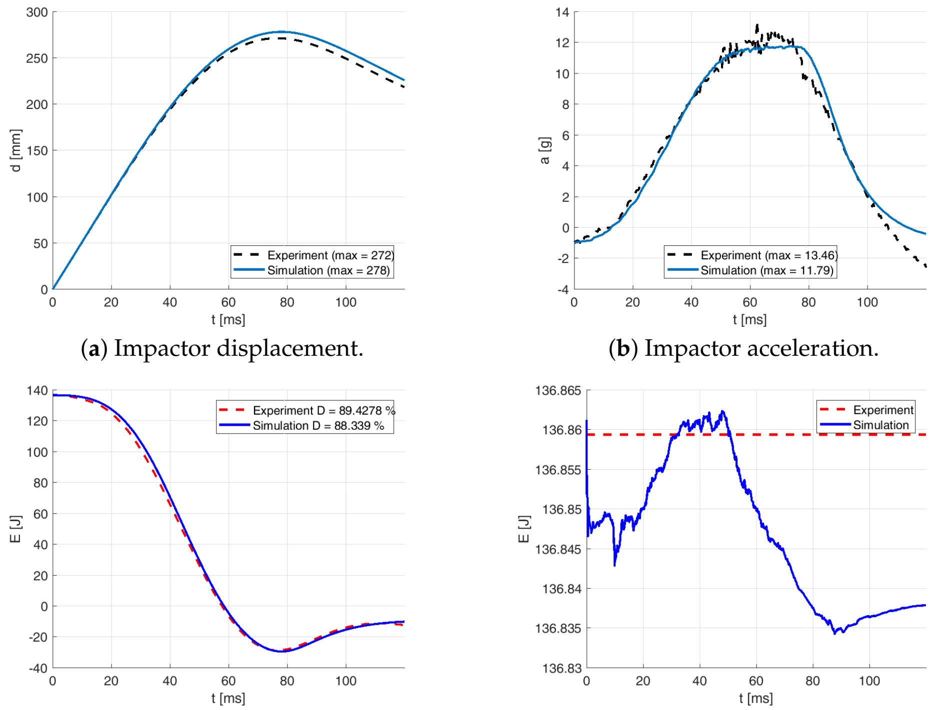

(**a**) Impactor displacement. (**b**) Impactor acceleration.

(**c**) Impactor energy loss. (**c**) Impactor total energy.

Figure 26. Comparison of drop test simulation to experiment for the drop height $H = 15$ dm and $n = 10$ layers: (**a**) Displacement (**b**) Acceleration. (**c**) Energy loss. (**d**) Total energy.

4. Discussion

The quasi-static experiments were performed in 2 perpendicular directions supported by measurements in 2 skewed directions. Although MD and TD exhibited different loading behavior, the measurements in the skewed directions support that there is not any unexpectable behavior during loading in any auxiliary direction.

Table 4 shows a good agreement with factory data of the quasi-static experimental test regarding the tensile stress in both directions. The break elongation is 30 % higher in TD and 43 % lower in MD comparing to the material data sheet in Table 1, which might be caused by the laboratory conditions and influenced by the specimen size. The experimental measurements also confirms the previous studies that LLDPE is stiffer in MD comparing to TD [3,5,6,15].

Table 5 summarizes the yield stresses $\sigma_y^{\mathrm{MD}} = 8.4$ MPa and $\sigma_y^{\mathrm{TD}} = 8$ MPa as well as the yield strains $\epsilon_y^{\mathrm{MD}} = 0.26$ and $\epsilon_y^{\mathrm{TD}} = 0.33$, which are comparable to the values presented by Durmus *et al.* (2008), who states the yield stress $\sigma_y = 9.9$ MPa and the yield strain $\epsilon = 0.33$. However, Durmus *et al.* (2008) measured the elongation at break equal to 1045 %, which is higher to those measured and stated by the material data sheet. The Young modulus in Table 6 $E = 50$ MPa shows also a comparable value to that published by Durmus *et al.* (2008), who identifies the Young modulus experimentally as $E = 64$ MPa.

The drop test experimental measurements prove considerable energy absorption summarized in Table 7, which was used in the constitutive material model for the dynamic response. To keep a stable optimization in MD and TD, the same multipliers were supposed for developing the dynamic constitutive material model in MD and TD. The optimized multipliers as well as optimization process errors are stated in Table 8. The optimization process leads to the stiffening about 3.5 times for the drop height H =10 dm as the stiffening is about 2 for the drop height H =15 dm. The yield stress balances around the measured quasi-static value.

The acceleration error was calculated just during the loading phase, because of the complex unloading behavior and because of the fact that the constitutive material model is being developed for the energy absorption during the loading.

The dynamic response exhibits similar values for both drop heights, so single dynamic constitutive material curves were developed by averaging the particular response curves in MD and TD. The averaged constitutive material curves in MD and TD were then used to recalculate all the drop test again with the error shown in Table 9. The developed constitutive material model describes well the LLDPE foil behavior to be used for energy absorption during the impact.

Even though the identified constitutive material model describes the expected scenario for the energy absorption, future work considers the identification of dynamic constitutive material curves for different loading patterns and different drop energy, which is also the limitation of the current study. Such future development would enable using the constitutive material model to be implemented for wider spectra of impact scenarios with energy absorption.

5. Conclusions

The paper contributes to the field of virtual testing by developing the material model and identifying its constitutive parameters. The target material was LLDPE, a material traditionally used for packaging goods to protect them during transportation. The paper proves a high energy absorption of the material suitable for impact protection, also due by its low weight. Both quasi-static and dynamic responses of the material were considered in the constitutive material model.

Besides the constitutive material parameter identification for both quasi-static and dynamic responses, the paper provides a complex description of the experimental measurements. While the quasi-static response is measured using a unilateral stretch measurement in MD and TD, the dynamic tests employ a sphere impact using the drop tower.

The quasi-static response is analyzed and evaluated based on the measurement of several samples providing the final curves describing the stress resultant dependent on the strain in MD and TD. Those quasi-static curves serve initial values for the dynamic response, which is optimized using aligning the experimental and calculated accelerations of the impactor.

A good agreement of experimental and model results was achieved and reported, providing the linear low-density polyethylene material model for virtual testing.

Author Contributions: Conceptualization, L.H.; data curation, L.H.; formal analysis, L.H., J.Š. and R.C.; funding acquisition, L.H.; investigation, P.K., T.B., J.Š, S.K., R.K. and L.H.; methodology, L.H. and J.Š.; project administration, L.H.; resources, P.K.; software, J.Š., L.H., R.C. and M.P.; supervision, L.H.; validation, L.H. and J.Š.; visualization, L.H.; writing–original draft preparation, L.H.; writing–review and editing, L.H., P.K., J.Š., T.B., R.K., S.K., R.C. and M.P. All authors have read and agreed to the published version of the manuscript.

Funding: This research was funded by the John H. and Amy Bowles Lawrence Foundation, by the European Regional Development Fund-Project grant number CZ.02.1.01/0.0/0.0/17_048/0007280, and by the University of West Bohemia grant number SGS-2019-002.

Acknowledgments: The authors thank to Mr Alojz Hanuliak for donating the testing material roll used for experiments.

Conflicts of Interest: The authors declare no conflict of interest. The funders had no role in the design of the study; in the collection, analyses, or interpretation of data; in the writing of the manuscript, or in the decision to publish the results'.

Abbreviations

The following abbreviations are used in this manuscript:

doi:10.20944/preprints202103.0589.v1

LLDPE	Linear low-density polyethylene
MD	Machine direction
TD	Transverse direction
D3	Skewed direction by 45^{o}
D4	Skewed direction by -45^{o}

References

1. Špička, J.; Hynčík, L.; Kovář, L.; Hanuliak, A. Virtual assessment of advanced safety systems for new mobility modes. 16^{th} International Symposium on Computer Methods in Biomechanics and Biomedical Engineering and the 4^{th} Conference on Imaging and Visualization; Columbia University: New York City, The United States, 2019; p. 263.
2. Hanuliak, A. Safety Restraint System for Motor Vehicles, 2018. Publication number: WO2018/219371.
3. Mezghani, K.; Furquan, S. Analysis of dart impact resistance of low-density polyethylene and linear low-density polyethylene blown films via an improved instrumented impact test method. *Journal of Plastic Film & Sheeting* **2012**, *28*, 298–313.
4. Ragaert, K.; Delva, L.; Van Damme, N.; Kuzmanovic, M.; Hubo, S.; Cardon, L. Microstructural foundations of the strength and resilience of LLDPE artificial turf yarn. *Applied Polymer Science* **2016**, *133*, 1–12.
5. Bosi, F.; Pellegrino, S. Molecular based temperature and strain rate dependent yield criterion for anisotropic elastomeric thin films. *Polymer* **2017**, *125*, 144–153.
6. Bosi, F.; Pellegrino, S. Nonlinear thermomechanical response and constitutive modeling of viscoelastic polyethylene membranes. *Mechanics of Materials* **2018**, *117*, 9–21.
7. Jeon, K.; Krishnamoorti, R. Morphological behavior of thin linear low-density polyethylene films. *Macromolecules* **2008**, *49*, 7131–7140.
8. Morris, B.A., 9. Strength, stifffness, and abuse resistance. In *The Science and Technology of Flexible Packaging*; Elsevier, 2017; pp. 309–350.
9. Omar, M.F.; Akil, H.M.; Ahmad, Z.A. Effect of molecular structures on dynamic compression properties of polyethylene. *Materials Science and Engineering A* **2012**, *538*, 125–134.
10. Jordan, J.; Casem, D.T.; Bradley, J.M.; Dwivedi, A.K. Mechanical Properties of Low Density Polyethylene. *Journal of Dynamic Behavior of Materials* **2016**, *2*, 411–420.
11. Zhang, X.M.; Elkoun, S.; Ajji, A.; Huneault, M.A. Oriented structure and anisotropy properties of polymer blown films: HDPE, LLDPE and LDPE. *Polymer* **2004**, *45*, 217–229.
12. Ren, Y.; Ying, Y.; Yao, X.; Y., T.; Z., L.L. Different Dependence of Tear Strength on Film Orientation of LLDPE Made with Different Co-Monomer. *Polymers* **2019**, *11*, 434.
13. Dogru, S.; Aksoy, B.; Bayraktar, H.; Alaca, B.E. Poisson's ratio of PDMS thin films. *Polymer Testing* **2018**, *69*, 375–384.
14. Dorigato, A.; Pegoretti, A.; Kolařík, J. Nonlinear tensile creep of linear low density polyethylene/fumed silica nanocomposites: Time-strain superposition and creep prediction. *Polymer Composites* **2010**, *31*, 1947–1955.
15. Krishnaswamy.; K., R.; Lamborn, M.J. Tensile Properties of Linear Low Density Polyethylene (LLDPE) Blown Films. *Polymer Engineering and Science* **2000**, *40*, 2395–2396.
16. Plaza, A.R.; Ramos, E.; Manzur, A.; Olayo, R.; Escobar, A. Double yield points in triblends of LDPE, LLDPE and EPDM. *Journal of Material Science* **1997**, *32*, 549–554.
17. Richeton, J.; Ahzi, S.; Daridon, L.; Rémond, Y. Modeling of strain rates and temperature effects on the yield behavior of amorphous polymers. *Journal de Physique IV (Proceedings)* **2003**, *110*, 39–44.
18. Luyt, A.S.; Gasmi, S.A.; Malik, S.S.; Aljindi, R.M.; Ouederni, M.; Vouyiouka, S.N.; Porfyris, A.D.; Pfaendner, R.; D., P.C. Artificial weathering and accelerated heat aging studies on low-density polyethylene (LDPE) produced via autoclave and tubular process technologies. *eXPRESS Polymer Letters* **2021**, *15*, 121–136.
19. Du, W.; Ren, Y.; Tang, Y.; Shi, Y.; Yao, X.; Zheng, C.; Zhang, X.; Guo, M.; Zhang, S.; Liu, L.Z. Different structure transitions and tensile property of LLDPE film deformed at slow and very fast speeds. *European Polymer Journal* **2018**, *103*, 170–178.
20. Omar, M.F. *Static and Dynamic Mechanical Properties of Thermoplastic Materials*; Lap Lambert Academic Publishing, 2013.
21. Durmus, A.; Kasgöz, A.; Macoscom, C.W. Mechanical Properties of Linear Low-density Polyethylene (LLDPE)/clay Nanocomposites: Estimation of Aspect Ratio and Interfacial Strength by Composite Models. *Macromolecular Science, Part B: Physics* **2008**, *47*, 608–619.
22. LLDPE Foils. http://www.tichelmann.cz/lldpe-folie, 2020. Accessed: 21 November 2020.
23. ASTM Standards. https://www.astm.org, 2021. Accessed: 17 March 2021.
24. ESI Group International. *VPS User's Manual*, 2020.
25. Cichos, D.; Otto, M.; Zoelsch, S.; Clausnitzer, S.; Vetter, D.; Pfeiffer, G.; de Vogel, D.; O., S. Crash Analysis Criteria Description. *Mechanics of Time-Dependent Materials* **2011**.
26. Gupalov, V.; Kukaev, A.; Shevchenko, S.; Shalymov, E.; Venediktov, V. Physical Principles of a Piezo Accelerometer Sensitive to a Nearly Constant Signal. *Sensors* **2018**, *18*, 3258.